Particle-hole thermalization in a composite superconducting and normal-conducting nanowire

L. E. Reichl ●* and F. Estrella ●

Center for Complex Quantum Systems and Department of Physics, The University of Texas at Austin, Austin, Texas 78712, USA

The mechanisms by which isolated condensed matter systems thermalize is a topic of growing interest. Thermalization is known to be linked to the emergence of chaos in the dynamics of a system. We show that a solid state scattering system, containing superconducting elements, can thermalize scattered states without affecting the degree of entanglement of the scattered states. We consider a composite $NSNSNSNSN$ nanowire composed of $Bi_2Sr_2CaCu_2O_{8+x}$ superconducting segments (S) and normal conducting segments (N). We consider parameter regimes where all current flow is due to tunneling currents that are facilitated by quasibound state resonances inside the $SNSNSNS$ structure. At certain energies, scattered pure states approach ergodicity, even though they remain pure.

I. INTRODUCTION

The mechanisms by which small quantum systems thermalize has been a topic of growing interest since the work of Srednicki [1], in which he derived the Maxwell-Boltzmann, Bose-Einstein, and Fermi-Dirac single particle distributions for a quantum hard sphere gas directly from the ergodicity of the gas (i.e., all energy eigenstates states on the energy surface are equally probable). This is called the *eigenstate thermalization hypothesis* [2–4].

More recently, Kaufman *et al.* [5] have shown that quantum thermalization can emerge locally in pure (unentangled) states of a small isolated quantum system due to a quench of the microscopic states of the system. They found that *the full quantum state* (of the system) *remains pure, whereas thermalization occurs on a local scale.* In the sections below, we show that a similar phenomenon can occur locally in an electron current that flows through a composite superconducting nanowire. For our system, at certain energies, the scattered states approach ergodicity, even though their degree of entanglement is not changed.

One of the most powerful indicators of the character of electron statistics, in currents flowing through solid state devices, is the measurement of cross-correlated shot noise in electron currents emerging from the devices. The measurement of positive cross-correlated shot noise is an indication that the electrons are showing bunching behavior similar to currents of bosonlike particles (like photons). A connection between positive electron shot noise and violation of Bell's inequalities [6] has been shown explicitly [7–9] using scattering theory. Shot-noise measurements have been used to observe electron bunching in a variety of systems with superconducting segments, where Cooper pairs provide the source of electron bunching. For example, there have been several studies of electron bunching in NSN

(normal-superconducting-normal) circuits [10–21] and in $NSNSN$ circuits [22,23]. For such circuits, current flow must be ballistic so phase coherence is maintained, and this is feasible in quasi-one-dimensional wires [24–27].

In the sections below, we focus on a composite *narrow* 3D nanowire, composed of four superconducting segments (S) separated by normal segments (N). The structure of the wire is $(NS)^4N$ (see Fig. 1). The nanowire is connected, at each end, to very low temperature thermal reservoirs. These thermal reservoirs are the source of the electron currents in the wire. We assume that the wire is narrow enough that current can only propagate in one channel. The dynamics of smaller versions of the composite wire (NSN) [12,13] and $NSNSN$ [22] have been studied using $La_{2-x}Sr_xCuO_4$ (LSCO) for the superconducting segments. The $NSNSN$ wire has also been studied [23] using $Bi_2Sr_2CaCu_2O_{8+x}$ (BSCCO) for the superconducting segments. We here focus on the $(NS)^4N$ nanowire using BSCCO for the superconducting segments because, as we will see, it shows an impressive degree of particle and hole bunching and thermalization of the currents that pass through it.

We begin Sec. II by determining parameters of the $(NS)^4N$ nanowire, which allows a single channel to be open in the wire and allows a tunneling current to exist in the wire. In Sec. III, we derive the scattering matrix and show the behavior of transmission and reflection coefficients for the wire, the structure of quasibound states, and the behavior of the current that flows through the wire. In Sec. IV, we show that a pure unentangled bipartite electron state, that scatters through the wire, remains pure but also becomes thermalized at certain energies. We also compute change in the entropy associated with the scattered state as a function of incident energy, and we find energy regimes where the scattering currents have thermalized and show signatures of chaos. In Sec. V, we introduce the cross-correlated shot noise and show that, for energy regimes where bipartite states appear to thermalize locally, the shot noise can become positive. In Sec. VI, we introduce a bipartite density matrix for the wire and use it

---

*reichl@mail.utexas.edu
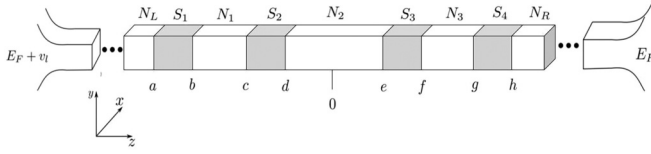
FIG. 1. The $(NS)^4N$ nanowire.

to test the concurrence of an entangled state as it transitions the wire. We also introduce an ensemble density matrix that allows us to analyze the scattering process in terms of a few modes and adds to the information we obtain from the shot noise. Finally, in Sec. VII, we make some concluding remarks.

II. PROPERTIES OF WIRE WITH BSCCO SEGMENTS

Some high T_c superconducting materials will allow current flow in a single propagating channel in ballistic nanowires if the width of the wire is comparable to the coherence length of the superconducting material [12]. One of these high-T_c superconductors is BSCCO [13]. BSCCO has a critical temperature $T_c = 96$ K, a superconducting gap $\Delta = 2.346 \times 10^{-21} J = 5.3814 \times 10^{-4}$ a.u. (the atomic unit of energy is 1 a.u. $= 4.38 \times 10^{-18} J$), and a coherence length $\xi = 1.6 \times 10^{-9}$ m $= 30.24$ a.u. (the atomic unit of length is 1 a.u. $= 5.2917 \times 10^{-11}$ m) [28].

In subsequent sections, we consider the nanowire shown in Fig. 1, which consists of a central $SNSNSNS$ composite wire, coupled to thermal reservoirs at each end via a normal conducting nanowire. As in Ref. [23], we assume that current in the wire flows along the z axis, and the wire has widths $L_x = 1.2 L_y = 7.62 \times 10^{-9}$ m $= 144$ a.u. These widths are greater than the coherence length of BSCCO and are consistent with propagation widths reported for normal wires in Ref. [27]. The Fermi velocity for BSCCO is $v_F = 1.118 \times 10^5 \frac{m}{s} = 5.112 \times 10^{-2}$ a.u. (the atomic unit of velocity is 1 a.u. $= 2.188 \times 10^6 \frac{m}{s}$), and the Fermi energy is $E_F = 5.69 \times 10^{-21} J = 0.001307$ a.u.

As described in Ref. [13], the source of electron currents in the wire is thermal reservoirs attached to the left and right ends of the wire. The Fermi distributions for particles [$N_p(e)$] and holes [$N_h(e)$] in the thermal reservoirs are

$$N_p(e) = N_h(e) = (1 + e^{e/k_B T})^{-1},$$

where e is the energy of a particle or hole measured relative to the Fermi energy (the true energy of particles is $E = E_F + e$ and of holes is $E = E_F - e$). Note that, for a given energy e, the same number of particles and holes are available to enter the wires. We require that the width of the energy interval, available to the holes and particles that are emitted from the thermal reservoirs, be

$$\delta e = 0.0004976 \text{ a.u.} \approx 0.0005 \text{ a.u.}$$

This energy interval only allows electrons and holes to propagate in the first conducting channel of the wire. The temperature for which the Fermi surface has this available width is $T_0 = 22.755$ K, which is well below the critical temperature for the BSCCO superconductor. A plot of the Fermi
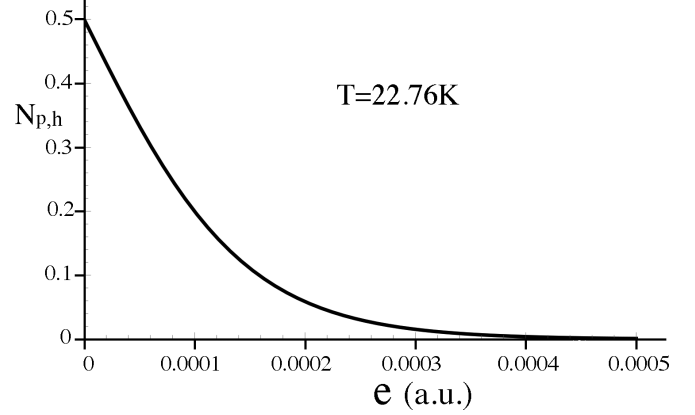
FIG. 2. A plot of the Fermi distribution for the thermal reservoir (with no bias) at $T = 22.76$ K.

distributions for particles $N_p(e)$ [holes $N_h(e)$] at temperature $T = 22.755$ K is shown in Fig. 2.

III. ELECTRON AND HOLE STATES IN THE NANOWIRE

The $(NS)^4N$ nanowire consists of three normal (N) and four superconducting (S) segments, $SNSNSNS$, attached to normal wires (N) at each end. The interfaces are located, from left to right, at $z = a$, $z = b$, $z = c$, $z = d$, $z = e$, $z = f$, $z = g$, $z = h$ (see Fig. 1).

In the subsequent discussion, the lengths of the four superconducting segments is fixed at $\Delta z_S = 200$ a.u. The lengths of the three interior normal conducting segments will be varied. The lengths of the left and right outer normal conducting segments in the $SNSNSNS$ structure, respectively, will be taken as $\Delta z_{N,L} = \Delta z_{N,R} = 20n$ a.u., where n is an integer that we vary so $35 \leqslant n \leqslant 45$. We will mostly focus on the value $n = 40$. The central normal segment will have lengths $\delta z_{N,C} = 40n$ a.u. and will be twice as long as the left and right normal segments.

The scattering wave function in the normal leads is

$$\bar{\Phi}_N(z) = \begin{bmatrix} \Phi_T^N(z) \\ \Phi_B^N(z) \end{bmatrix} = \frac{A_p^I}{\sqrt{q_p}} \begin{bmatrix} 1 \\ 0 \end{bmatrix} e^{iq_p z} + \frac{A_h^I}{\sqrt{q_h}} \begin{bmatrix} 0 \\ 1 \end{bmatrix} e^{-iq_h z}$$
$$+ \frac{A_p^O}{\sqrt{q_p}} \begin{bmatrix} 1 \\ 0 \end{bmatrix} e^{-iq_p z} + \frac{A_h^O}{\sqrt{q_h}} \begin{bmatrix} 0 \\ 1 \end{bmatrix} e^{+iq_h z}, \quad (1)$$

where A_p^I (A_p^O) are amplitudes of incoming (outgoing) particle states, and $A_h^I (A_h^O)$ are amplitudes of incoming (outgoing) hole states. The wave vectors, q_p and q_h are defined as

$$q_p = \sqrt{2(E_F + e)} \quad \text{and} \quad q_h = \sqrt{2(E_F - e)}, \quad (2)$$

where E_F is the Fermi energy and e is the particle or hole energy measured relative to the Fermi energy.

The states in the superconducting regions are obtained using Bogoliubov-deGennes theory for superconductors [29]. The particle-hole states in the interior superconducting
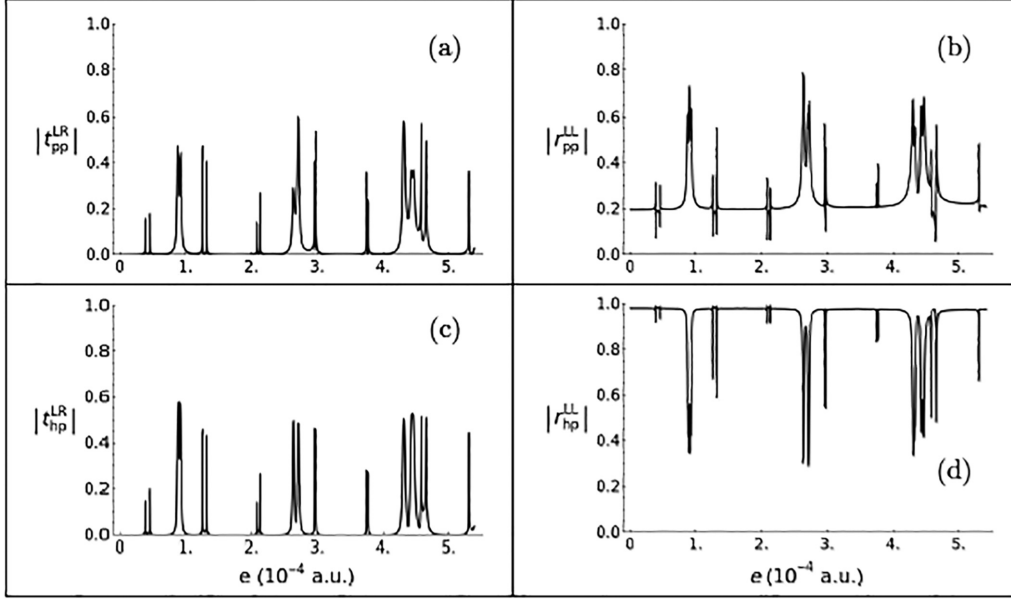
FIG. 3. Scattering amplitudes for energies $0 \leqslant e \leqslant 5 \times 10^{-4}$ a.u. (a) $|t_{pp}^{LR}|$, (b) $|r_{pp}^{LL}|$, (c) $|t_{hp}^{LR}|$, and (d) $|r_{hp}^{LL}|$.

regions can be written

$$\bar{\Phi}_S(z) = \begin{bmatrix} \Phi_T^S(z) \\ \Phi_B^S(z) \end{bmatrix} = \frac{A_p^S}{\sqrt{k_p}} \begin{bmatrix} u_o \\ v_o \end{bmatrix} e^{ik_p z} + \frac{B_h^S}{\sqrt{k_h}} \begin{bmatrix} v_o \\ u_o \end{bmatrix} e^{-ik_h z}$$
$$+ \frac{C_p^S}{\sqrt{k_p}} \begin{bmatrix} u_o \\ v_o \end{bmatrix} e^{-ik_p z} + \frac{D_h^S}{\sqrt{k_h}} \begin{bmatrix} v_o \\ u_o \end{bmatrix} e^{+ik_h z}, \qquad (3)$$

where A_p^S (C_p^S) is the amplitude of particles that propagate to the right (left), and B_h^S (D_h^S) is the amplitude of holes that propagate to the right (left). The wave vectors, k_p and k_h, are defined as

$$k_p = \sqrt{2}\sqrt{E_F + \sqrt{e^2 - \Delta^2}} \text{ and } k_h = \sqrt{2}\sqrt{E_F - \sqrt{e^2 - \Delta^2}}, \qquad (4)$$

where E_F is the Fermi energy, Δ is the superconducting gap, and e is the particle or hole energy measured relative to the Fermi energy. The quantities u_o and v_o are defined

$$u_o = \frac{1}{\sqrt{2}}\sqrt{1 + \frac{\sqrt{e^2 - \Delta^2}}{e}} \text{ and } v_o = \frac{1}{\sqrt{2}}\sqrt{1 - \frac{\sqrt{e^2 - \Delta^2}}{e}}. \qquad (5)$$

A. The scattering matrix

The normal and superconducting segments are linked by equating both states and derivatives of states at the interfaces. However, for the *NSNSNSNSN* structure, if this is not done systematically, the process can become extremely complex. We have found that it is useful to introduce two pods, one that describes the normal segments and another that describes the superconducting segment. The method for obtaining the S matrix from the pods is discussed in Appendix A.

The S matrix relates the outgoing amplitudes to the incoming amplitudes, so

$$\bar{\Phi}_A^O = \bar{\bar{S}} \cdot \bar{\Phi}_A^I.$$

where

$$\bar{\Phi}_A^{I(O)} = \left\{ \left\{ A_{p,L}^{I(O)} \right\}, \left\{ A_{h,L}^{I(O)} \right\}, \left\{ A_{p,R}^{I(O)} \right\}, \left\{ A_{h,R}^{I(O)} \right\} \right\}. \qquad (6)$$

The scattering matrix can be written

$$\bar{\bar{S}} = \begin{pmatrix} r_{pp}^{LL} & r_{ph}^{LL} & t_{pp}^{LR} & t_{ph}^{LR} \\ r_{hp}^{LL} & r_{hh}^{LL} & t_{hp}^{LR} & t_{hh}^{LR} \\ t_{pp}^{RL} & t_{ph}^{RL} & r_{pp}^{RR} & r_{ph}^{RR} \\ t_{hp}^{RL} & t_{hh}^{RL} & r_{hp}^{RR} & r_{hh}^{RR} \end{pmatrix}, \qquad (7)$$

where $r_{i,j}^{LL}$ and $r_{i,j}^{RR}$ (with $i = p, h$ and $j = p, h$) denote reflection probability amplitudes on the left and right, respectively, and $t_{i,j}^{RL}$ and $t_{i,j}^{LR}$ denote transmission probability amplitudes for propagation from left to right and right to left, respectively. The energies of particles and holes are each measured relative to the Fermi energy E_F, so the actual difference in energy of a particle and hole, each with energy e, is $2e$. Because of the existence of Cooper pairs in the superconducting material, a particle can reflect from the superconductor as a hole (and vice versa) (a process known as Andreev reflection [30]). Additionally, an incident particle can transmit through to the other side as a hole and vice versa. This is known as crossed Andreev reflection.

The particles (and holes) come from the thermal reservoirs at the left and right ends of the nanowire. The particles and holes must tunnel through the superconducting segments and propagate through the normal segments to transit the nanowire because all the electrons coming from the thermal reservoirs have energy less than that of the superconducting gap. However, we find that there are certain energies at which the particles and holes set up quasibound state structures with finite lifetimes, in the nanowire, and these quasibound states allow transmission of a current through the nanowire.

In Fig. 3, we plot the scattering amplitudes for energies $0 \leqslant e \leqslant 0.0005$ a.u. and for $0.00008 \leqslant e \leqslant 0.0001$ a.u. These plots show that particles can only transmit through the wire at discrete energies. These are energies at which
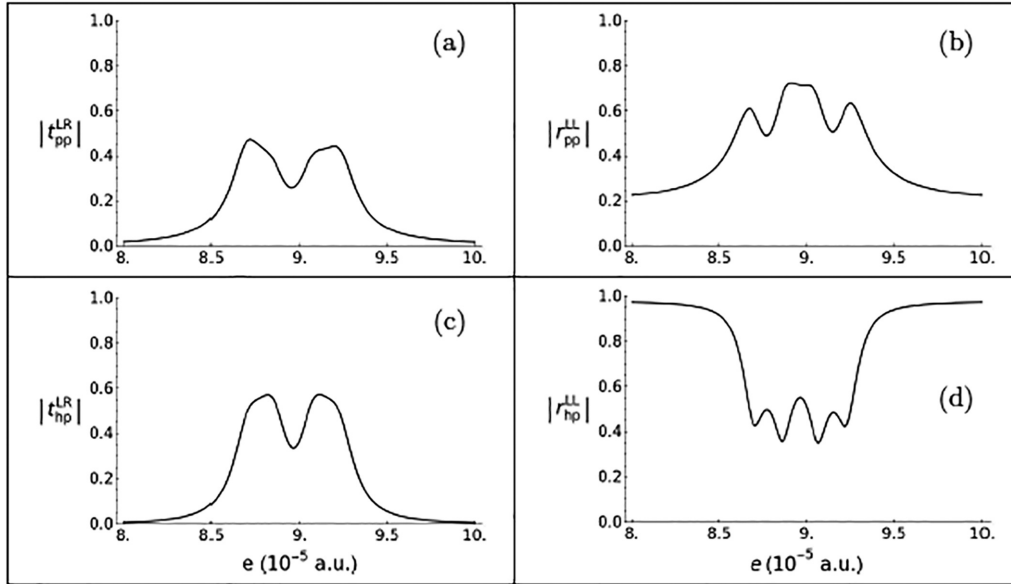
FIG. 4. Scattering amplitudes for energies $8 \times 10^{-5} a.u. \leqslant e \leqslant 10 \times 10^{-5}$ a.u. (a) $|t_{pp}^{LR}|$, (b) $|r_{pp}^{LL}|$, (c) $|t_{hp}^{LR}|$, and (d) $|r_{hp}^{LL}|$.

quasibound states form in the wire. In Fig. 4, we show the scattering amplitudes in the energy interval $0.00008 \leqslant e \leqslant 0.0001$, which will be the main focus of the subsequent discussion. In this energy interval, there is significant activity in the wire and sufficient electron flow from the thermal reservoir to make it interesting. In Fig. 5, we show the complex
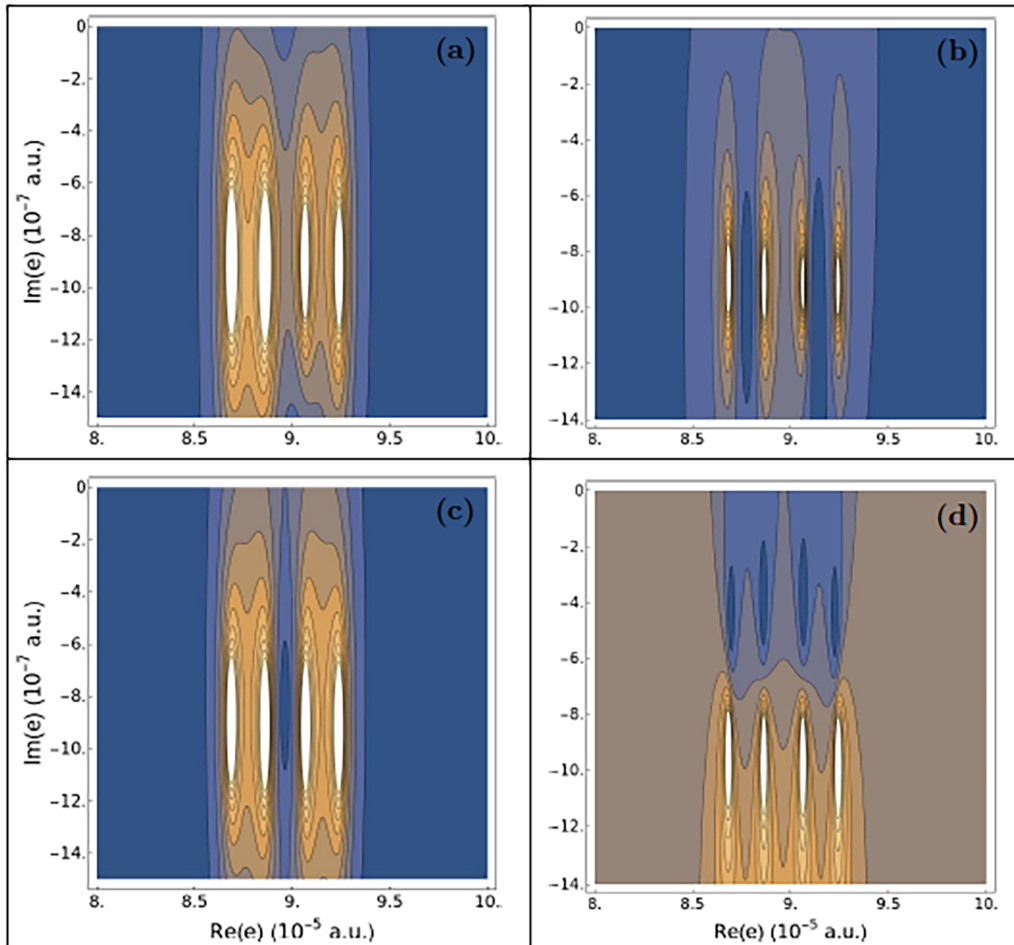

FIG. 5. Poles for energies 8×10^{-5} a.u. $\leqslant \text{Re}[e] \leqslant 10 \times 10^{-5}$ a.u. (a) $|t_{pp}^{LR}|$, (b) $|r_{pp}^{LL}|$, (c) $|t_{hp}^{LR}|$, and (d) $|r_{hp}^{LL}|$.
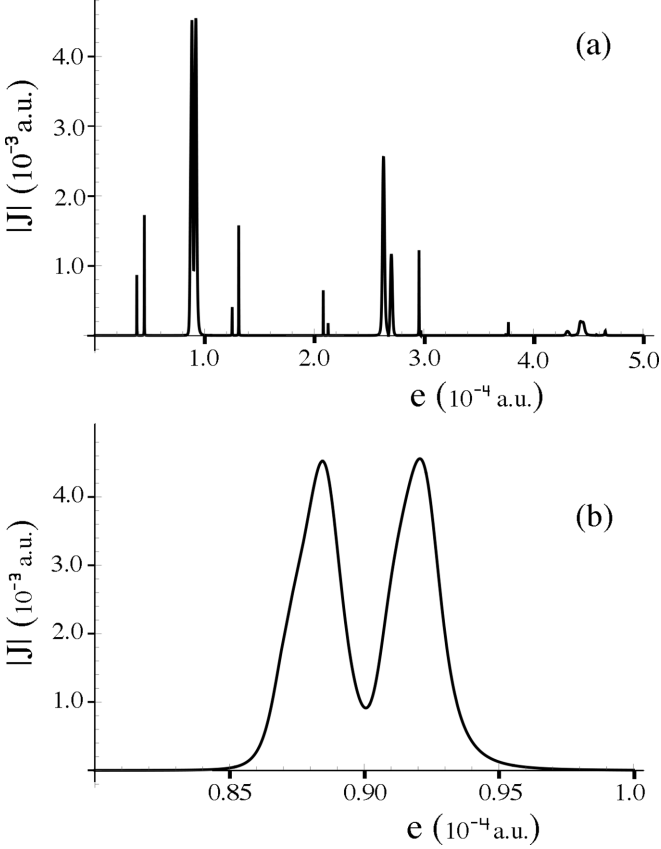
FIG. 6. (a) A plot of $|J|$ for $0 \leqslant e \leqslant 5 \times 10^{-4}$ a.u. (a) A plot of $|J|$ for $0.8 \leqslant e \leqslant 1.0 \times (10^{-4}$ a.u.). For both plots the bias was $v_p = -v_h = 0.00002$.

poles associated with the quasibound states in the energy interval $0.00008 \leqslant e \leqslant 0.0001$. The quasibound states have lifetimes of approximately $\tau = \mathrm{Im}(e)/\hbar \approx 10^{-10} s$ and allow conduction through the wire.

In Fig. 6, we plot the current through the wire for energies $0 \leqslant e \leqslant 0.0005$. The wire allows the current to flow at the same energies that allow formation of quasibound states.

IV. THERMALIZATION OF PARTICLE AND HOLE STATES

Let us now consider the dynamical effect of the *SNSNSNS* scattering structure on the particles and holes that tunnel through it. There are resonant energies at which tunneling can occur because of quasibound particle-hole states that are set up inside the *SNSNSNS* segment of the wire. We will focus on the particles and holes that enter the wire in the energy interval $0.00008 \leqslant e \leqslant 0.0001$. As we can see from Fig. 6, there is a significant amount of current flowing through the wire in the energy interval $0.000085 \leqslant e \leqslant 0.000095$, and this is exactly the energy interval where the quasibound states most strongly affect the scattering amplitudes.

A. Monopartite states

We can monitor the dynamics of particles or holes as they tunnel through the *SNSNSNS* structure. We denote incident states by the row vectors

$$\bar{\Phi}_A^I = \left\{ \Phi_A^I(1), \Phi_A^I(2), \Phi_A^I(3), \Phi_A^I(4) \right\}$$
$$= \left\{ A_{pL}^I, A_{hL}^I, A_{pR}^I, A_{hR}^I \right\}, \tag{8}$$

where A_{pL}^I and A_{hL}^I (A_{pR}^I and A_{hR}^I) denote amplitudes of particles and holes incident from the left (right). We denote the outgoing states by the row vectors

$$\bar{\Phi}_A^O = \{\Phi_A(1), \Phi_A(2,), \Phi_A(3), \Phi_A(4)\}$$
$$= \{A_{pL}, A_{hL}, A_{pR}, A_{hR}\}. \tag{9}$$

The amplitudes of outgoing states are denoted A_{pL} and A_{hL} (A_{pR} and A_{hR}). In Fig. 7, we show the absolute value of the amplitudes $|\Phi(j)|$ of states that emerge from the *SNSNSNS* structure, as a function of energy, when the state $\Phi_A^I(1), = A_{pL}^I$ is incident at that given energy. Figure 7(a) shows the incident state. Figures 7(b)–7(l) show states that emerge from the *SNSNSNS* structure at the indicated energies. For energies $e = 0.000080 - 0.000085$ and energies $e = 0.000095 - 0.0001$, the scattered states are dominated by Andreev reflection (a particle enters from the left and is reflected as a hole to the left). However, for energies $e = 0.000086 \leqslant 0.000094$, different patterns emerge. For energies $e = 0.000088$ and 0.000091, for example, the largest amplitudes correspond to crossed Andreev reflection, where particle enters from the left and emerges as a hole on the right, although all three other possibilities have a large probability of occurring.

In Fig. 8, we show similar plots for the case when the hole state $\Phi_A^I(2), = A_{hL}^I$ enters from the left. Again, for energies $e = 0.000080 - 0.000085$ and $e = 0.000095 - 0.0001$ the scattering is dominated by Andreev reflection where a hole enters from the left and is reflected to the left as a particle. For energies $e = 0.000088$ and 0.000091, the largest amplitudes correspond to crossed Andreev reflection, where a hole enters from the left and emerges as a particle on the right.

Let us again consider the monopartite states $\bar{\Phi}_A = \{A_{pL}, A_{hL}, A_{pR}, A_{hR}\}$. Each state has four components. If each component of a given state has equal probability of $P(j) = 1/4$, where $j = 1, ..., 4$, the (dimensionless) entropy [31] associated with this monopartite ergodic state is

$$S_{\mathrm{erg}} = -\sum_{j=1}^{4} P(j) \ln[P(j)] = 1.3863. \tag{10}$$

We can compute the entropy associated with the state shown in Fig. 7, as a function of energy. The probability of the jth component of the outgoing state is given by $|\Phi(j)|^2$. The entropy associated with the outgoing states is

$$S = -\sum_{j=1}^{4} |\Phi(j)|^2 \ln[|\Phi(j)|^2]. \tag{11}$$

At energy $e = 0.000088$, all four of the outgoing states have significant probability and the entropy of the outgoing states is $S_{\mathrm{out}} = 1.3642$, which is about 98% of true ergodicity S_{erg}. The entropy associated with the outgoing states in Fig. 7, as a function of energy, is shown in Fig. 9. We see that for energies $e = 0.000088$ and $e = 0.000092$, the entropy is within 98% of true ergodicity S_{erg} for the initial condition $\Phi^I(3) = A_{pL}^I$. If we compute the entropy associated with each of the three other incident monopartite states, we get the same result.

FIG. 7. (a) Incident state $A_{pL}^{I} = 1$ at each energy. (b)–(l) Absolute value of outgoing state amplitudes at the energies indicated in the figure.
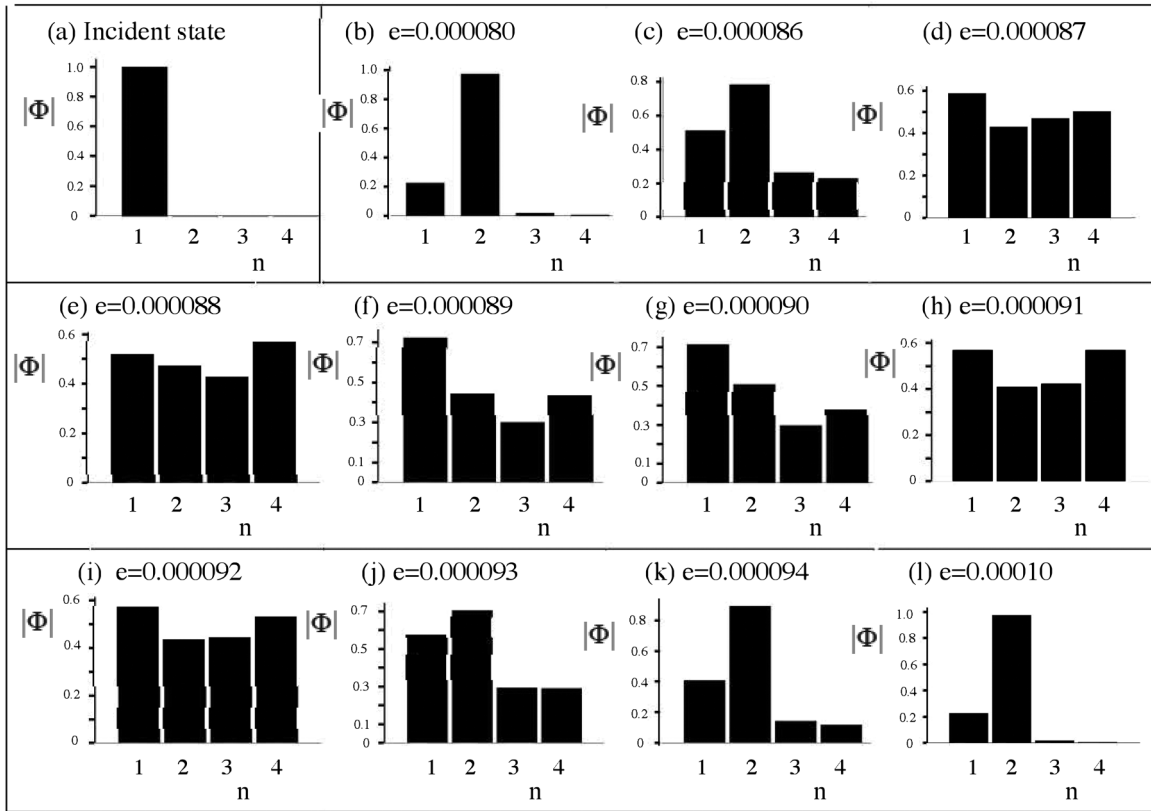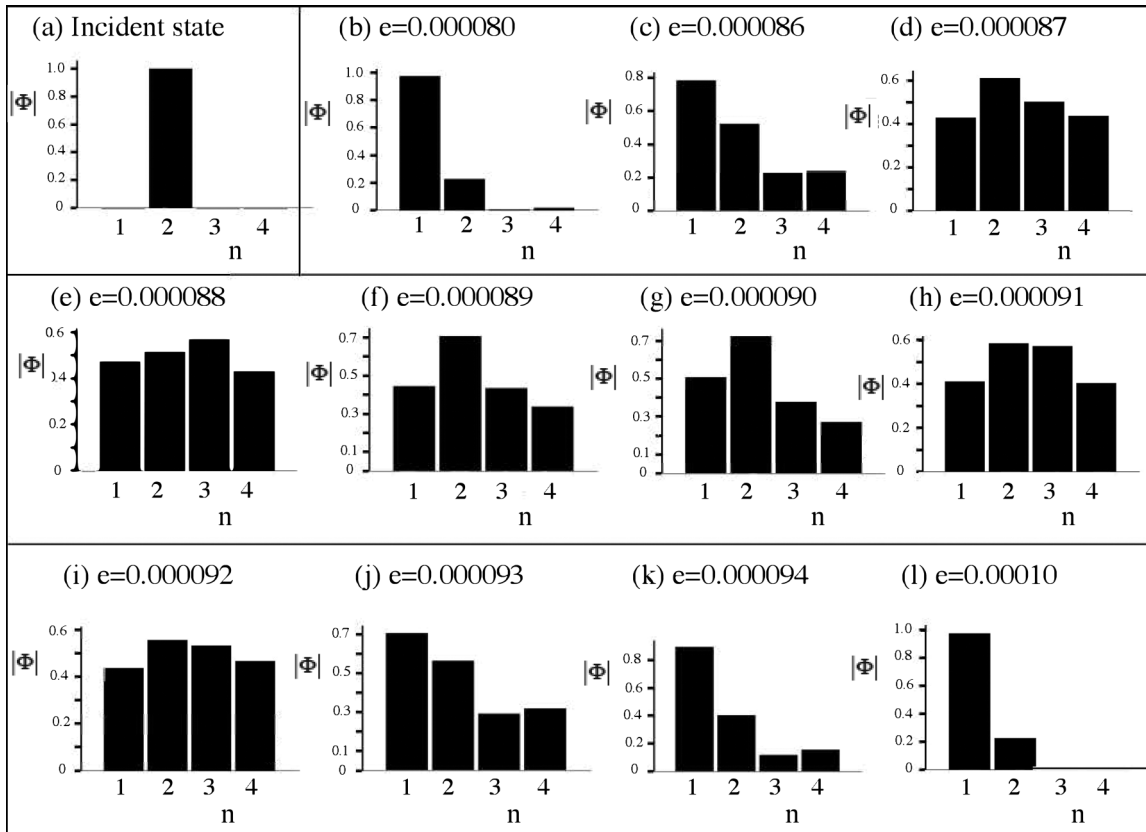

FIG. 8. (a) Incident state $A_{hL}^{I} = 1$ at each energy. (b)–(l) Absolute value of outgoing state amplitudes at the energies indicated in the figure.
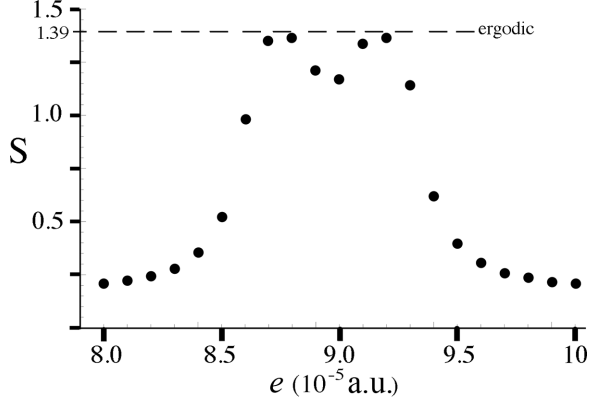
FIG. 9. Entropy of outgoing states for incident monopartite state $A^I_{pL} = 1$ at each energy. In the figure, there are two different energies where the outgoing states are within 2% of being rigorously ergodic.

B. Bipartite states

We can form bipartite states for the *NSNSNSNSN* system if we first introduce a new set of states, $\bar{\Phi}^I_B$ and $\bar{\Phi}^O_B$, with the same structure as $\bar{\Phi}^I_A$ and $\bar{\Phi}^O_A$ except $A \rightarrow B$. We can think of these as Alice (the A states) and Bob (the B states) sending in electrons and holes from the outer normal regions. The bipartite states are normalized to one and can be written $\bar{\Phi} = \bar{\Phi}^A \otimes \bar{\Phi}^B$, where $\otimes$ denotes the Kronecker product.

The incident bipartite states have 16 components, which we denote as the column vector:

$$
\begin{aligned}
\bar{\Phi}_I = \big\{ & \big\{A^I_{pL}B^I_{pL}\big\}, \big\{A^I_{pL}B^I_{hL}\big\}, \big\{A^I_{pL}B^I_{pR}\big\}, \big\{A^I_{pL}B^I_{hR}\big\}, \\
\times\ & \big\{A^I_{hL}B^I_{pL}\big\}, \big\{A^I_{hL}B^I_{hL}\big\}, \big\{A^I_{hL}B^I_{pR}\big\}, \big\{A^I_{hL}B^I_{hR}\big\}, \\
\times\ & \big\{A^I_{pR}B^I_{pL}\big\}, \big\{A^I_{pR}B^I_{hL}\big\}, \big\{A^I_{pR}B^I_{pR}\big\}, \big\{A^I_{pR}B^I_{hR}\big\}, \\
\times\ & \big\{A^I_{hR}B^I_{pL}\big\}, \big\{A^I_{hR}B^I_{hL}\big\}, \big\{A^I_{hR}B^I_{pR}\big\}, \big\{A^I_{hR}B^I_{hR}\big\} \big\}.
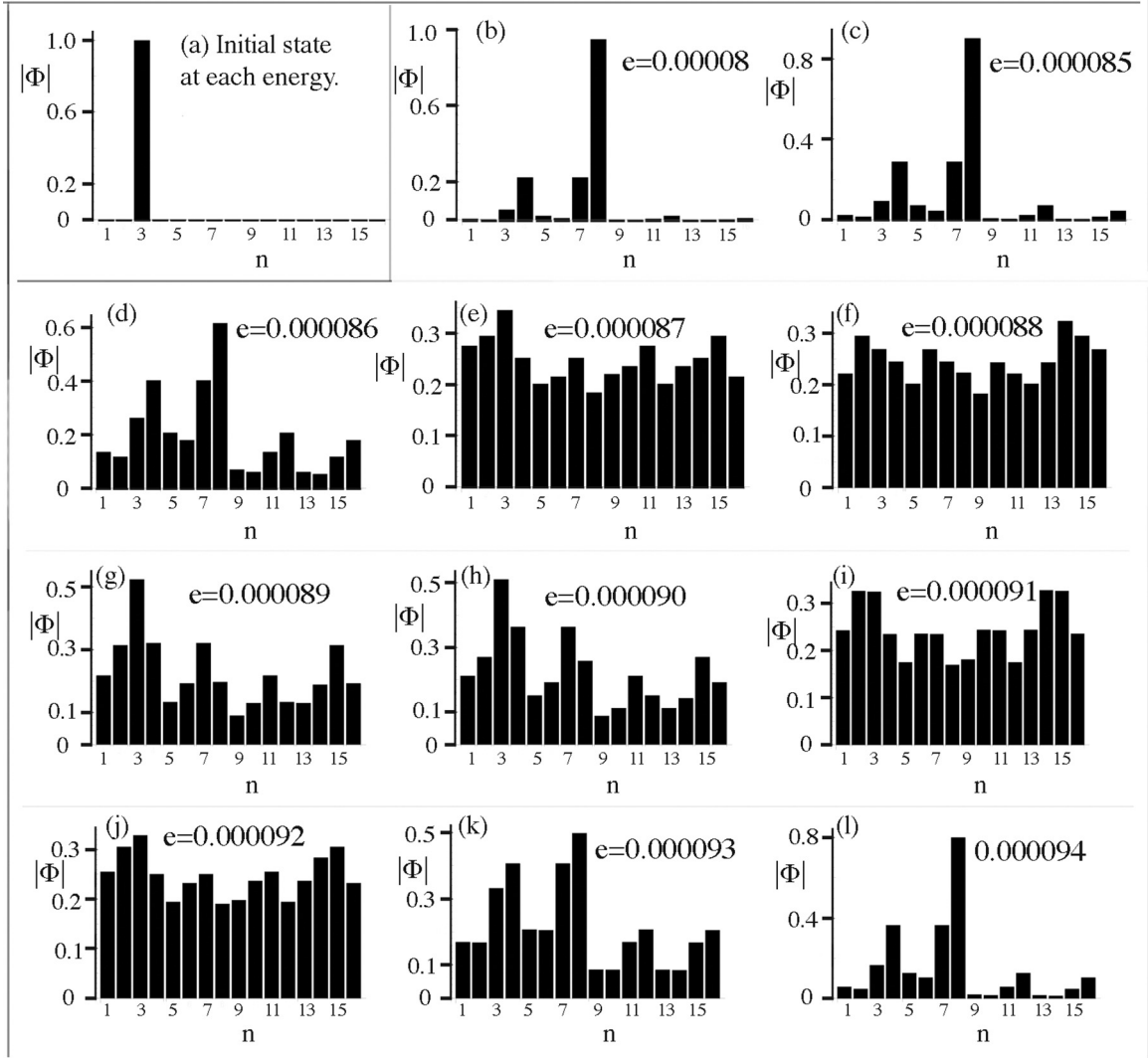\end{aligned}
\tag{12}
$$

FIG. 10. (a) The incident state $\Phi_I(3) = A^I_{pL}B^I_{pR} = 1$. (b)–(l) The outgoing states at the energies indicated in the figure. The states for higher energies $0.000095 \leqslant 0.0001$ look again like the state in (b).

The outgoing bipartite states have the same structure and, in subsequent plots, are numbered from left to right from 1 to 16.

C. Entropy of scattered bipartite states

Let us now consider the case where one particle enters the *SNSNSNS* region from the left and another particle enters from the right. The incident state (transposed) is

$$(\bar{\Phi}^I)^T = \{\{0, 0, 1, 0, 0, 0, 0, 0, 0, 0, 0, 0, 0, 0, 0, 0\}\}, \quad (13)$$

where $\Phi^I(3) = A_{pL}^I B_{pR}^I$. The outgoing states, for a range of energies, are shown in Fig. 10. For energies $0.00008 \leqslant .000085$, the scattering is dominated by Andreev reflection [30]. The incident particles are reflected as holes on their respective sides. There is a much smaller contribution where one particle reflects as a hole and the other as a particle. The energies $e = 0.000087$, $e = 0.000088$, $e = 0.000091$, and $e = 0.000092$ are particularly striking because they appear to *approach* ergodicity. For ergodic systems, all outgoing states with the same energy are equally probable (this is a signature of underlying chaos). However, for all energies shown in Fig. 10, the incoming and outgoing states are separable; they are not entangled (as we show below).

If we introduce any of the other incident states $\Phi^I(j)$, we see a similar behavior in the outgoing states. For each incident pure state, all 16 possible components of the corresponding outgoing state has significant probability for energies $e = 0.000087$, $e = 0.000088$, $e = 0.000091$, and $e = 0.000092$. In fact, they are close to being rigorously ergodic, even though for each case the states are pure and separable at all energies. If each component of a given state has a probability of

$P(j) = 1/16$, where $j = 1, ...16$, the (dimensionless) entropy associated with this bipartite state is

$$S_{\mathrm{erg}} = -\sum_{j=1}^{16} P(j)\ln[P(j)] = 2.773. \quad (14)$$

If we plot the entropy of the state shown in Fig. 10 as a function of energy, it has the same structure as for the monopartite incident states in Fig. 9, but for the bipartite states it is twice as large.

D. Entropy of scattered tri- and quadripartite states

We can analyze the entropy of outgoing states for incident tripartite and quadripartite states. For the incident tripartite state $\Phi^I = A_{pL}^I B_{pL}^I C_{pL}^I$ (Alice, Bob, and Carol each send in a particle from the left), there are 64 outgoing states. If they all have equal probability (are ergodic), the entropy associated with the outgoing states would be $S_{\mathrm{erg}} = -\ln[\frac{1}{64}] = 4.15889$, which is three times the ergodic entropy of the monopartite states. A plot (not shown here) of the entropy associated with the outgoing states, as a function of energy, is identical to Fig. 9, except three times as large.

For the quadripartite incident state $\Phi^I = A_{pL}^I B_{pL}^I C_{pL}^I D_{pL}^I$ (Alice, Bob, Carol, and David each send in a particle from the left), there are 256 outgoing states. If they all have equal probability (are ergodic), the entropy associated with the outgoing states would be $S_{\mathrm{erg}} = -\ln[\frac{1}{256}] = 5.54518$, which is four times the ergodic monopartite entropy. A plot of the entropy (not shown here) associated with the outgoing quadripartite states, as a function of energy, is identical to the monopartite case, but four times as large. It is of interest to
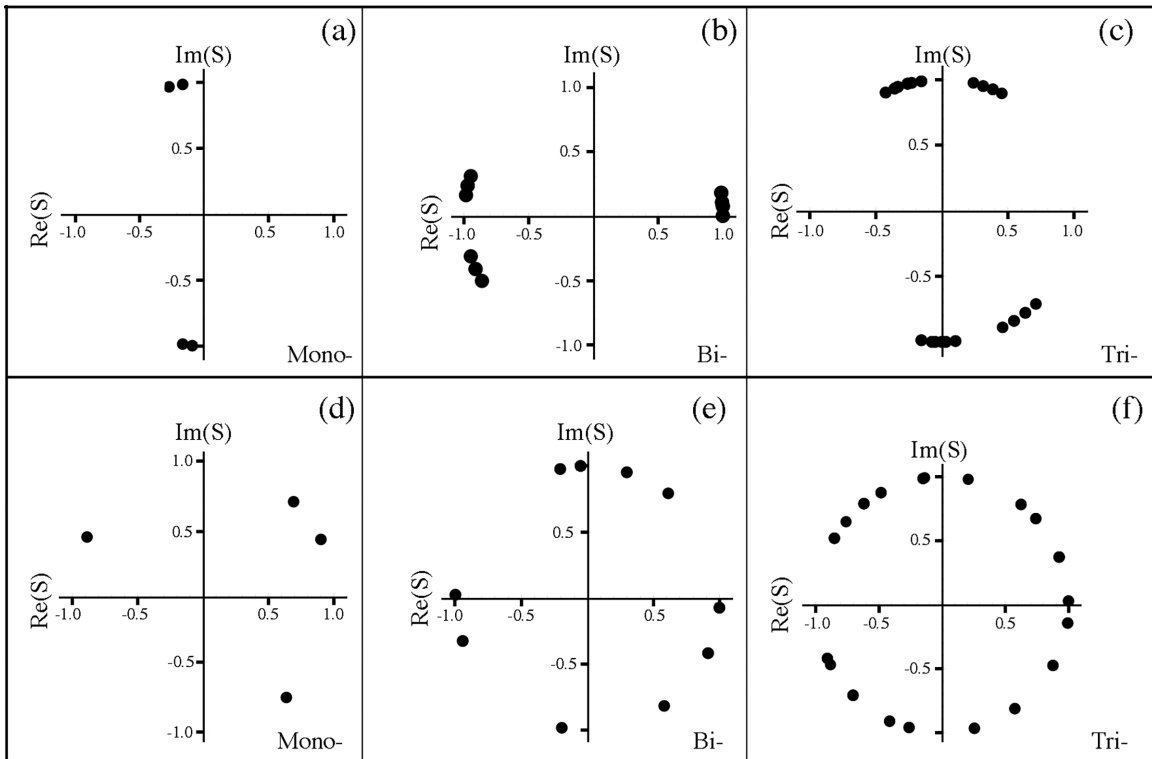

FIG. 11. *S*-matrix eigenvalue spectrum. (a) Monopartite system for $e = 0.000080$, (b) bipartite system for $e = 0.000080$, (c) tripartite system for $e = 0.000080$, (d) monopartite system for $e = 0.000092$, (e) bipartite system for $e = 0.000092$, (f) tripartite system for $e = 0.000092$.

note that in all four cases (monopartite, bipartite, tripartite, and quadripartite), the states that approach ergodicity are not entangled.

E. A signature of chaos in the scattering phases

For scattering systems, there is another signature of underlying chaos (other than ergodicity) which was originally introduced by Wigner (for Hamiltonian systems) to try to explain nuclear scattering data [3,32,33]. Wigner assumed that the underlying Hamiltonian in the scattering system could be represented by a random matrix, a Gaussian orthogonal ensemble (GOE). This is based on the assumption that all symmetries are broken, except the universal symmetries. This idea was later applied to scattering matrices by Dyson, who proposed a scattering matrix whose eigenphases are uniformly distributed on the unit circle [34], forming a circular orthogonal ensemble (COE). The connection between the GOE behavior of the Hamiltonian of a closed system and the COE behavior of the corresponding open system has been discussed in Refs. [35–37].

We have analyzed the behavior of the scattering matrix for monopartite, bipartite, and tripartite states in the *SNSNSNS* scattering system. In each case, the eigenvalues of the S matrix lie on the unit circle. Plots of these eigenvalues are shown in Fig. 11 for energies $e = 0.000080$ and $e = 0.000092$ (energies with the lowest and highest entropy in Fig. 9). While there is some degeneracy in both cases, we find that the eigenvalues are clustered together for energy $e = 0.000080$ and they spread almost uniformly on the unit circle for $e = 0.000092$. This gives another indication that the scattering dynamics is showing manifestations of chaos at energies where the entropy is largest and the system appears to be approaching ergodicity.

V. CROSS-CORRELATED SHOT NOISE

Cross-correlated shot noise is the name given to the thermal average of correlations between fluctuations about the average current, in the left and right outer normal leads. It contains useful information about the electron dynamics that is not available from conduction experiments [38,39]. For systems with superconducting segments, it can reveal energy regimes where the electron statistics become bosonlike due to pairing induced by Cooper pairs in the superconducting segments [40]. As discussed in Refs. [40], the presence of disorder can also enhance positive shot noise in electronic circuits.

The cross-correlated shot noise can be written

$$S^{LR}(z, y; t, s) = \tfrac{1}{2}\langle (J_L(z, t) - \langle J_L \rangle_{\text{th}})(J_R(y, s) - \langle J_R \rangle_{\text{th}}) \\ + (J_R(y, s) - \langle J_R \rangle_{\text{th}})(J_L(z, t) - \langle J_L \rangle) \rangle_{\text{th}}, \tag{15}$$

where $J_L(z, t)$ [$J_R(z, t)$] is the current in the left (right) outer normal lead. The averages $\langle \rangle_{\text{th}}$ are thermal averages taken with respect to the Fermi distributions of the left and right thermal reservoirs.

We have evaluated the correlations between fluctuations in the currents leaving the left end at $z = \mathsf{a}$ and the right end at $z = \mathsf{h}$. We first take the Fourier transform of Eq. (15) and keep the zero frequency limit, which we denote $\tilde{S}^{LR}(\omega = 0)$. The zero frequency limit of the shot noise can be written explicitly in the form $\tilde{S}^{LR}(\omega = 0) = \int de \, dS_{\text{tot}}^{LR}(e)$, where $dS_{\text{tot}}^{LR}(e)$ is the total differential cross correlated shot noise. The differential shot noise $dS_{\text{tot}}^{LR}(e)$ has been shown to contain explicit information about the statistical nature of particles and holes leaving the left and right sides of the central *SNSNSNS* component of the $(NS)^4N$ device.
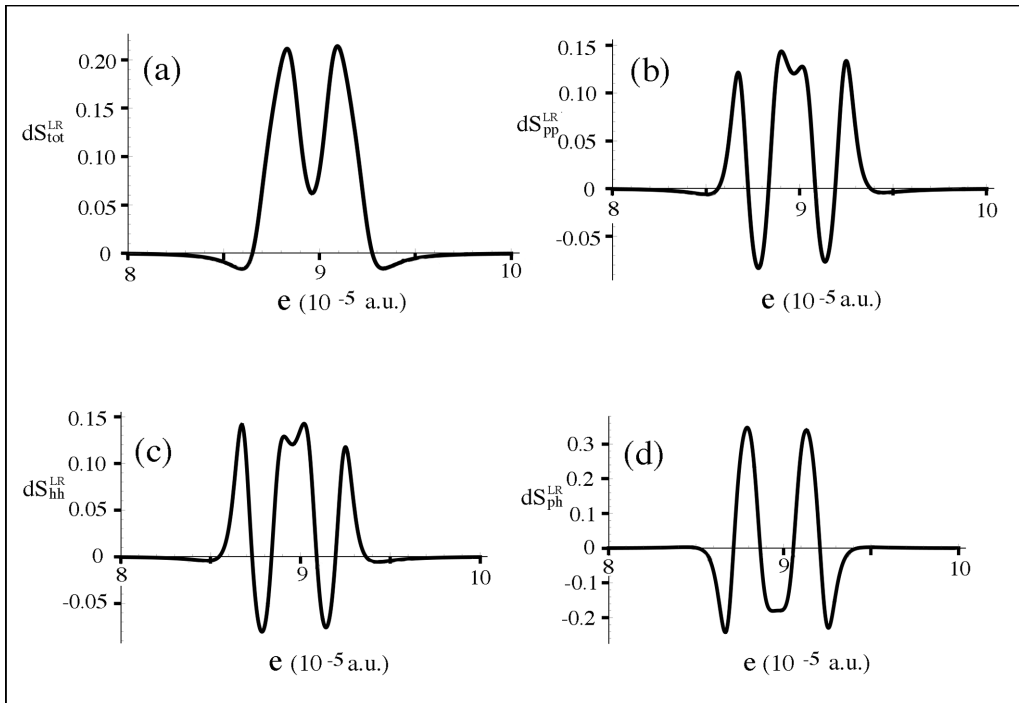

FIG. 12. Plots of the shot noise for energies $0.00008 \leqslant e \leqslant 0.0001$. (a) Total shot noise. (b) Particle-particle shot noise. (c) Hole-hole shot noise. (d) Particle-hole shot noise.
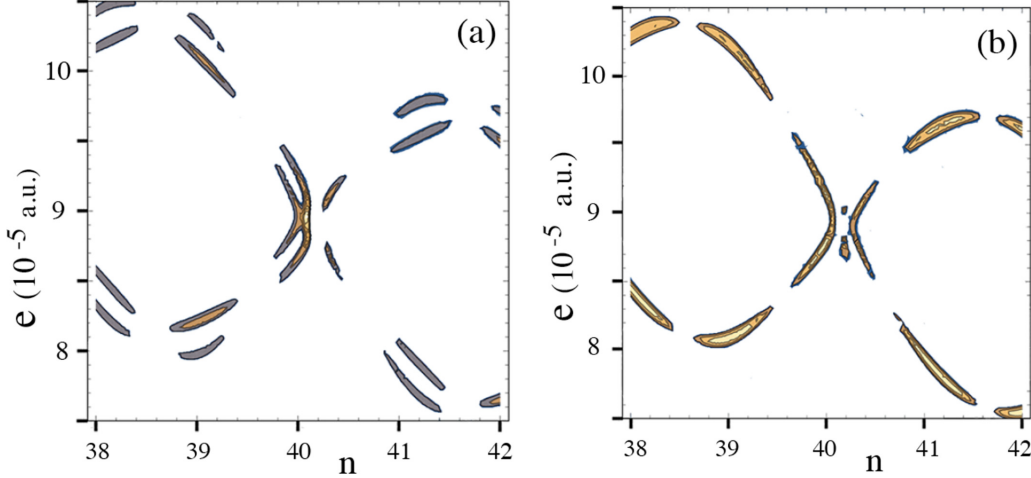
FIG. 13. (a) Particle-particle shot noise map. (b) Particle-hole shot noise map. The superconducting segments each have length $\Delta z = 200$ a.u. The left and right inner normal segments have length $\Delta z = 100 + 20n$ a.u. The central normal segment has length $\Delta z = 200 + 40n$ a.u.

It is useful to decompose $dS_{\text{tot}}^{LR}(e)$ in terms of contributions from pp, hh, and ph processes, so

$$dS_{\text{tot}}^{LR}(e) = dS_{pp}^{LR}(e) + dS_{hh}^{LR}(e) + dS_{ph}^{LR}(e). \qquad (16)$$

Explicit expressions for $dS_{pp}^{LR}(e)$, $dS_{pp}^{LR}(e)$, and $dS_{pp}^{LR}(e)$ are given in Appendix C. In Fig. 12, we plot $dS_{\text{tot}}^{LR}(e)$, $dS_{pp}^{LR}(e)$, $dS_{hh}^{LR}(e)$, and $dS_{ph}^{LR}(e)$ for the energy interval $0.00008 \leqslant e \leqslant 0.0001$. The total shot noise [Fig. 12(a)] is positive for most of this energy interval and has a shape very similar to the entropy curve in Fig. 11. However, when we decompose the total shot noise in terms of the pp, hh, and ph contributions, we see that the pp and hh contributions are mutually exclusive to the ph contribution. Energy intervals with strong pp and hh positive shot noise have negative ph shot noise, while energy intervals with strong ph shot noise have negative pp and hh shot noise.

In Fig. 13, we show contour plots of values of $dS_{pp}^{LR}(e)$ [Fig. 13(a)] and of $dS_{ph}^{LR}(e)$ [Fig. 13(b)] (where they become positive) for a range of energies e and a range of normal segment sizes (with the superconducting segments lengths fixed at 200 a.u.). The regions where the pp shot noise is positive are different from the regions where the ph shot noise is positive. Thus, it appears that energies for which particle-particle pairs exhibit bosonic behavior (bunching) occurs at different energies and segment sizes than that of particle-hole pairs. The bunching of electrons and holes indicates that they emerge more closely spaced than classical or fermionic particles. This localized (in energy) bosonic behavior of the particles and holes (which are fermions) is due to the Cooper pairing of the electrons and holes inside the superconducting segments and, as mentioned in Ref. [40], may be enhanced by the ergodicity of the scattered particles and holes at those energies.

VI. DENSITY MATRIX FOR BIPARTITE STATES

The density matrix for the *SNSNSNS* scattering system provides a means for determining the degree of entanglement of states flowing through the wire and also provides a simpler

alternative to the shot noise for locating device parameters that give rise to particle and hole bunching. Here we will only consider the density matrix for bipartite states, but it could also be constructed for tripartite and quadripartite states if needed.

A. Entanglement measures

The *SNSNSNS* scattering structure does not entangle states that pass through it, but it does maintain the degree of entanglement of states that pass through it, even as it radically changes the composition of those states. Let us consider the example of the incident bipartite entangled state:

$$\Phi^I = \frac{1}{\sqrt{2}}(\Phi(3) + \Phi(9)) = \frac{1}{\sqrt{2}}\left(A_{pL}^I B_{pR}^I + A_{pR}^I B_{pL}^I\right). \qquad (17)$$

As discussed by Hill and Wootters [41,42] and by Rungta *et al.* [43], a measure of the degree of entanglement based on the density matrix, $\hat{\rho} = \Phi \cdot \Phi^\dagger$, is the *concurrence*, $\mathcal{C}$. For bipartite systems, one computes concurrence $\mathcal{C} = \sqrt{2(1 - \text{Tr}[\rho_B^2])}$, where ρ_B is the reduced density matrix for Bob (obtained by taking the trace of $\hat{\rho}$ with respect to Alice states). For an unentangled bipartite state, $\mathcal{C} = 0$. If the state Φ^I is entangled, then $\mathcal{C} > 0$.

For the state considered in Fig. 7, $\mathcal{C} = 0$ for both the incident state and the outgoing state, even at energies where the outgoing state is 98% ergodic.

The incident entangled state considered in Eq. (17) has a concurrence $\mathcal{C} = 1.0$. After the incident entangled state has passed through *SNSNSNS*, the structure of the outgoing state has changed drastically but its generalized concurrence remains constant at $\mathcal{C} = 1.0$. The *SNSNSNS* device does not change the degree of entanglement of states that pass through it.

B. Ensemble density matrix

We now form a density matrix, $\bar{\bar{\rho}}_{\text{tot}} = \bar{\Phi} \cdot \bar{\Phi}^\dagger$, from an ensemble of incoming bipartite states. There are various ways

to do this. We here consider a subset of eight members of the "incoming" set,

$$\left(A^I_{p,L}B^I_{p,L}, \quad A^I_{p,L}B^I_{p,R}, \quad A^I_{p,R}B^I_{p,L}, \quad A^I_{p,R}B^I_{p,R},\right.$$
$$\left.A^I_{h,L}B^I_{h,L}, \quad A^I_{h,L}B^I_{h,R}, \quad A^I_{h,R}B^I_{h,L}, \quad A^I_{h,R}B^I_{h,R}\right), \qquad (18)$$

each contributing with equal probability. Such an ensemble will smooth out the fluctuations in the probability distributions of outgoing states and give an average behavior of the system. The submatrix $\bar{\bar{\rho}}_1$ associated with the first member of the subset $A^I_{p,L}B^I_{p,L}$ is found by setting $A^I_{p,L} = A^{I*}_{p,L} = 1$
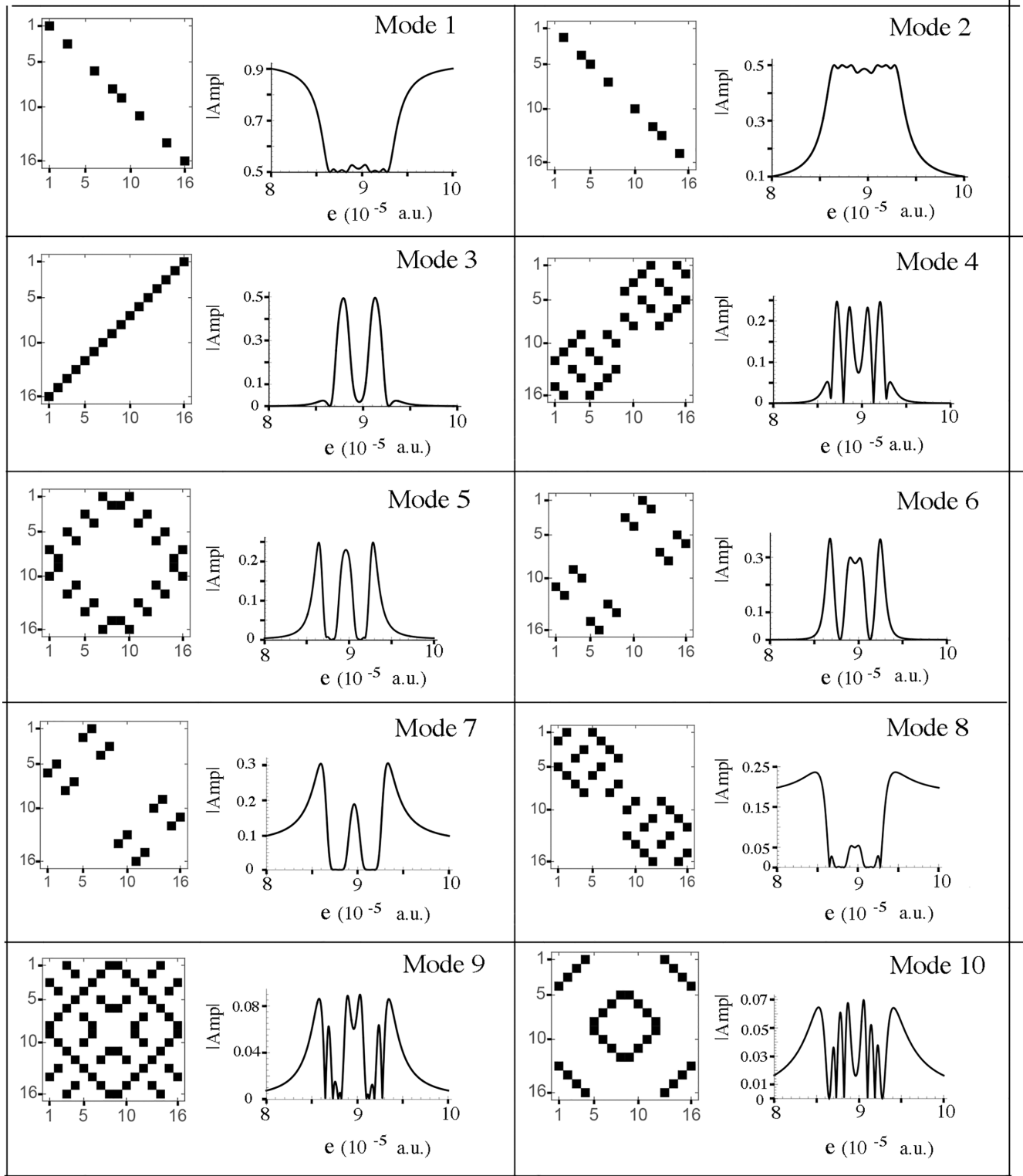

FIG. 14. The ten scattering modes for the *NSNSNSNSN* structure. For each mode, the right-hand figure gives $|\text{Amp}| \equiv 8|\rho[[i,j]]|$ (as a function of energy e), where $\rho[[i,j]]$ is any one of the matrix elements shown in black on the left.

TABLE I. Scattering mode structure (mode 1 contributes at each energy but is not explicitly listed).

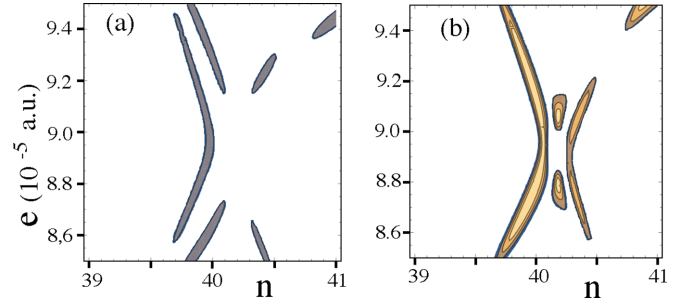| Energy (e)	Modes
0.000081 – 0.000084	8
0.000085	2, 7, 8
0.000086	2, 7
0.000087	2, 4, 6
0.000088	2, 3
0.000089	2, 6
0.000090	2, 5, 6
0.000091	2, 3
0.000092	2, 3, 4, 6
0.000093	2, 5, 7
0.000094	2, 7, 8
0.000095 – 0.000099	8

FIG. 15. (a) Contour plot of $\rho[[7, 1]]$, showing regions of energy and segment size where particle-particle and hole-hole entanglement dominates. (b) Contour plot of $\rho[[16, 1]]$, showing regions of energy and segment size where particle-hole entanglement dominates. The superconducting segments each have length $\Delta z = 200$ a.u. The left and right inner normal segments have length $\Delta z = 100 + 20n$ a.u. The central normal segment has length $\Delta z = 200 + 40n$ a.u.

and $B_{p,L}^I = B_{p,L}^{I*} = 1$ and setting all other incident amplitudes equal to zero. This gives a 16×16 submatrix $\bar{\bar{\rho}}_1$ of the density matrix which only depends on scattering amplitudes. We repeat this process for each member of the set in Eq. (18). The resulting eight submatrices add up to a density matrix $\bar{\bar{\rho}} = \frac{1}{8} \sum_{i=1}^{8} \bar{\bar{\rho}}_i$ for the ensemble. This density matrix has trace equal to one and 16 eigenvalues, eight of them equal to $\frac{1}{8}$ and eight of them equal to zero.

When we plot the *absolute value* of the 256 matrix elements of the density matrix, $\bar{\bar{\rho}}$, we find a very interesting result. The 256 plots we obtain are composed of only ten different structures (which we call modes). In Fig. 14, we show the absolute value of the ensemble density matrix elements and the energy variation of the absolute values (note we are plotting $|Amp| = 8|\rho_{rd}[[i, j]]|$). Eight of these modes (modes 1–8) dominate the scattering process because their amplitudes reach values greater than 0.2 The values of $|Amp|$ for the remaining two modes (modes 9 and 10) remain below 0.07.

The scattering modes (other than mode 1) that dominate at the various energies $0.000081 \leqslant e \leqslant 0.000099$ are listed in Table I. For energies $e = 0.00008$ and $e = 0.0001$, only mode 1 contributes significantly. For energies $0.000081 \leqslant e \leqslant 0.000084$ and $0.000095 \leqslant e \leqslant 0.000099$, it appears that mode 8 (and mode 1) dominates the scattering process. It is between energies $e = 0.000085$ and $e = 0.000094$ that the interesting behavior occurs, and it is between these energies that the shot noise becomes positive, indicating significant bunching of the particles. Note that, for energies $e = 0.000088$ and $e = 0.000091$, the scattering is dominated by modes 2 and 3, and these are precisely the energies for which the particle-hole shot noise peaks. Also, around energies $e = 0.0000865$, $e = 0.000090$, and $e = 0.000093$, modes 5–7 dominate. These are energies where the particle-particle and hole-hole shot noise dominates.

It is interesting to note that the change in the mode structure of the reduced density matrix, as energy of the scattering process is changed, appears to correlate directly to the change in the regions of positive shot noise as energy is changed. In Fig. 15(a), we show a contour plot of $\rho[[7, 1]]$, as a function of energy and segment size. It has an identical structure to the *pp*

shot noise map in Fig. 13(a). In Fig. 15(b), we show a contour plot of $\rho[[16, 1]]$ as a function of energy and segment size. It shows regions of energy and segment size where particle-hole bunching dominates. It has an identical structure to the *ph* shot noise map in Fig. 13(b). Thus, the density matrix appears to map out, explicitly, parameter regions where *pp*, *hh*, and *ph* bunching occurs as electrons pass through the *SNSNSNS* structure.

VII. CONCLUSIONS

We have analyzed current flow in the BSCCO *NSNSNSNSN* nanowire for a parameter regime in which only a single channel is open and only tunneling currents can transmit through the wire. The current flows at energies where electron-hole quasibound states can be set up inside the *SNSNSNS* structure of the wire. The electrons and holes must tunnel through the superconducting segments but can set up standing waves inside the normal segments internal to the *SNSNSNS* structure at certain discrete energies. We find that there are some energy regimes where *ph* currents emerging from opposite ends of the device are bosonic (while *pp* and *hh* currents are fermionic) and other energy regimes where the *pp* and *hh* currents that emerge are bosonic (while *ph* currents are fermionic). At these energies, there appears to be increased disorder in the scattering process as shown by ergodiclike behavior of the scattered particles (this was also observed in Ref. [40]).

We have analyzed the behavior of the degree of entanglement of incident entangled bi-partite states as they pass through the *NSNSNSNSN* structure. We find that the degree of entanglement of incident states remains unchanged as the states transition through the wire, although the composition of the states can change drastically and for some resonant energies appear to become thermalized (ergodic).

The shot-noise analysis of the scattering process and an analysis in terms of an ensemble density matrix give agreement in predicting energy regimes in which *ph* pairs (particle-hole pairs) become bosonic (rather than fermionic), and energy regimes in which *pp* and *hh* pairs become bosonic. However, the analysis in terms of the ensemble density matrix

gives much more detailed information about the scattering processes leading to bosonization of particles and holes exiting the wire.

One of the most interesting and surprising results of this paper is that, at energies that allow (tunneling) current flow through the wire, the scattering process though the composite *NSNSNSNSN* structure leads to a thermalization of the scattered current. At certain energies, while the incident current may consist of only a pair of incident particles, the outgoing current consists of all possible outgoing pairs with approximately the same probability, i.e., the outgoing current appears to be ergodic and therefore has become thermalized.

ACKNOWLEDGMENT

APPENDIX A: DERIVATION OF THE *S* MATRIX

The normal and superconducting segments of the nanowire are linked by equating both states and derivatives of states at the interfaces. It is useful to introduce two pods, one that describes the normal segments and another that describes the superconducting segment. To this end, we define

$$
\bar{\Upsilon}^N(z) = \begin{bmatrix} \Phi_T^N(z) \\ d\Phi_T^N(z) \\ \Phi_B^N(z) \\ d\Phi_B^N(z) \end{bmatrix} \quad \text{and} \quad \bar{\Upsilon}^S(z) = \begin{bmatrix} \Phi_T^S(z) \\ d\Phi_T^S(z) \\ \Phi_B^S(z) \\ d\Phi_B^S(z) \end{bmatrix}, \quad \text{(A1)}
$$

where, for the normal states, $d\Phi_T^N(z) = \frac{d\Phi_T^N(z)}{dz}$ and $d\Phi_B^N(z) = \frac{d\Phi_B^N(z)}{dz}$. Similarly, for the superconducting states $d\Phi_T^S(z) = \frac{d\Phi_T^S(z)}{dz}$ and $d\Phi_B^S(z) = \frac{d\Phi_B^S(z)}{dz}$.

We can connect the left side of the *left* inner normal segment to the right side of the *left* inner normal segment $\bar{\Upsilon}^N(\mathsf{b}) = \bar{\mathcal{V}}_{\mathsf{b,c}} \cdot \bar{\Upsilon}^N(\mathsf{c})$, where the matrix that connects them is given by

$$
\bar{\mathcal{V}}_{\mathsf{b,c}} = \begin{bmatrix} P_{1,\mathsf{b,c}} & P_{2,\mathsf{b,c}} & 0 & 0 \\ P_{3,\mathsf{b,c}} & P_{4,\mathsf{b,c}} & 0 & 0 \\ 0 & 0 & H_{1,\mathsf{b,c}} & H_{2,\mathsf{b,c}} \\ 0 & 0 & H_{3,\mathsf{b,c}} & H_{4,\mathsf{b,c}} \end{bmatrix}. \quad \text{(A2)}
$$

The eight nonzero matrix elements of the matrix $\bar{\mathcal{V}}_{\mathsf{b,c}}$ are given in Appendix B. Similarly, we can connect the left side and right sides of the central and of the right normal segments via the matrix equations $\bar{\Upsilon}^N(\mathsf{d}) = \bar{\mathcal{V}}_{\mathsf{d,e}} \cdot \bar{\Upsilon}^N(\mathsf{e})$ and $\bar{\Upsilon}^N(\mathsf{f}) = \bar{\mathcal{V}}_{\mathsf{f,g}} \cdot \bar{\Upsilon}^N(\mathsf{g})$.

In a similar manner, we can link the superconducting segments to the normal segments. For example, we require that the wave functions (and derivatives of wave functions) of the left outer normal conductor and leftmost superconducting segment be equal at $z = \mathsf{a}$. Similarly, we can link the *leftmost* superconducting segment to the leftmost inner normal region by requiring that the wave functions and derivatives of their wave functions be equal at $z = \mathsf{b}$. We then link the left outer normal region to the leftmost inner normal region by requiring that the coefficients A_p^S, C_p^S, B_h^S, and D_h^S be equal in the two sets

of equations. This gives $\bar{\Upsilon}^N(\mathsf{a}) = \bar{\mathcal{W}}_{\mathsf{a,b}} \cdot \bar{\Upsilon}^N(\mathsf{b})$, where

$$
\bar{\mathcal{W}}_{\mathsf{a,b}} = \begin{bmatrix} W_{1,\mathsf{a,b}} & W_{2,\mathsf{a,b}} & W_{3,\mathsf{a,b}} & W_{4,\mathsf{a,b}} \\ X_{1,\mathsf{a,b}} & X_{2,\mathsf{a,b}} & X_{3,\mathsf{a,b}} & X_{4,\mathsf{a,b}} \\ Y_{1,\mathsf{a,b}} & Y_{2,\mathsf{a,b}} & Y_{3,\mathsf{a,b}} & Y_{4,\mathsf{a,b}} \\ Z_{1,\mathsf{a,b}} & Z_{2,\mathsf{a,b}} & Z_{3,\mathsf{a,b}} & Z_{4,\mathsf{a,b}} \end{bmatrix}. \quad \text{(A3)}
$$

The 16 coefficients in the matrix $\bar{\mathcal{W}}_{\mathsf{a,b}}$ contain information about the leftmost superconducting segment and are given in Appendix B.

Similarly, we link the states in the left inner normal region to those in the central normal region and get $\bar{\Upsilon}^N(\mathsf{c}) = \bar{\mathcal{W}}_{\mathsf{c,d}} \cdot \bar{\Upsilon}^N(\mathsf{d})$. We link the states in the central normal region to those in the right inner normal region and get $\bar{\Upsilon}^N(\mathsf{e}) = \bar{\mathcal{W}}_{\mathsf{e,f}} \cdot \bar{\Upsilon}^N(\mathsf{f})$. And, finally, we link the states in the inner right normal region to those in the right outer normal region and get $\bar{\Upsilon}^N(\mathsf{g}) = \bar{\mathcal{W}}_{\mathsf{g,h}} \cdot \bar{\Upsilon}^N(\mathsf{h})$. The 16 elements of the matrices $\bar{\mathcal{W}}_{\mathsf{a,b}}$, $\bar{\mathcal{W}}_{\mathsf{c,d}}$, $\bar{\mathcal{W}}_{\mathsf{e,f}}$, and $\bar{\mathcal{W}}_{\mathsf{g,h}}$ are given in Appendix B.

We can now link the left and right normal conducting sides of the $(NS)^4N$ wire to obtain

$$
\bar{\Upsilon}^N(\mathsf{a}) = \bar{\bar{\mathcal{T}}}_{\mathsf{a,h}} \cdot \bar{\Upsilon}^N(\mathsf{h}), \quad \text{(A4)}
$$

where the matrix

$$
\bar{\bar{\mathcal{T}}}_{\mathsf{a,h}} = \bar{\mathcal{W}}_{\mathsf{a,b}} \cdot \bar{\mathcal{V}}_{\mathsf{b,c}} \cdot \bar{\mathcal{W}}_{\mathsf{c,d}} \cdot \bar{\mathcal{V}}_{\mathsf{d,e}} \cdot \bar{\mathcal{W}}_{\mathsf{e,f}} \cdot \bar{\mathcal{V}}_{\mathsf{f,g}} \cdot \bar{\mathcal{W}}_{\mathsf{g,h}} \quad \text{(A5)}
$$

is the transfer matrix for the $(NS)^4N$ wire. We now write

$$
\bar{\Upsilon}^N(\mathsf{a}) = \begin{bmatrix} \frac{1}{\sqrt{q_p}}\left(A_{p,L}^I e^{+iq_p\mathsf{a}} + A_{p,L}^O e^{-iq_p\mathsf{a}}\right) \\ i\sqrt{q_p}\left(A_{p,L}^I e^{+iq_p\mathsf{a}} - A_{p,L}^O e^{-iq_p\mathsf{a}}\right) \\ \frac{1}{\sqrt{q_h}}\left(A_{h,L}^I e^{-iq_h\mathsf{a}} + A_{h,L}^O e^{+iq_h\mathsf{a}}\right) \\ i\sqrt{q_h}\left(A_{h,L}^O e^{+iq_h\mathsf{a}} - A_{h,L}^I e^{-iq_h\mathsf{a}}\right) \end{bmatrix} \quad \text{(A6)}
$$

with a similar equation for $\bar{\Upsilon}^N(\mathsf{h})$. We then can obtain the *S* matrix from the equation for the transfer matrix. The *S* matrix connects the amplitudes of the incoming states to the amplitudes of the outgoing states. If we solve Eq. (A4) for the outgoing amplitudes in terms of the incoming amplitudes, we obtain

$$
\bar{\Phi}_A^O = \bar{\bar{S}} \cdot \bar{\Phi}_A^I,
$$

where

$$
\bar{\Phi}_A^{I(O)} = \left\{\left\{A_{p,L}^{I(O)}\right\}, \left\{A_{h,L}^{I(O)}\right\}, \left\{A_{p,R}^{I(O)}\right\}, \left\{A_{h,R}^{I(O)}\right\}\right\}. \quad \text{(A7)}
$$

The *S* matrix is shown explicitly in Eq. (7).

APPENDIX B: ELEMENTS OF THE MATRICES $\bar{\mathcal{V}}_{\mathsf{b,c}}$ AND $\bar{\mathcal{W}}_{\mathsf{a,b}}$

(a) The eight elements of the matrix $\bar{\mathcal{V}}_{\mathsf{b,c}}$ are given by

$$
P_{1,\mathsf{b,c}} = \cos(q_p(\mathsf{b}-\mathsf{c})), \quad P_{2,\mathsf{b,c}} = \frac{\sin(q_p(\mathsf{b}-\mathsf{c}))}{q_p},
$$

$$
P_{3,\mathsf{b,c}} = -q_p\sin(q_p(\mathsf{b}-\mathsf{c})), \quad P_{4,\mathsf{b,c}} = \cos(q_p(\mathsf{b}-\mathsf{c})),
$$

$$
H_{1,\mathsf{b,c}} = \cos(q_h(\mathsf{b}-\mathsf{c})), \quad H_{2,\mathsf{b,c}} = \frac{\sin(q_h(\mathsf{b}-\mathsf{c}))}{q_h},
$$

$$
H_{3,\mathsf{b,c}} = -q_h\sin(q_h(\mathsf{b}-\mathsf{c})), \quad H_{1,\mathsf{b,c}} = \cos(q_h(\mathsf{b}-\mathsf{c})).
$$

(b) The 16 matrix elements of the matrix $\bar{\bar{\mathcal{W}}}_{\mathsf{a},\mathsf{b}}$ are given by

$$W_{1,\mathsf{a},\mathsf{b}} = \frac{u_o^2 \cos{(k_p(\mathsf{a}-\mathsf{b}))}}{(u_o^2 - v_o^2)} - \frac{v_o^2 \cos{(k_h(\mathsf{a}-\mathsf{b}))}}{(u_o^2 - v_o^2)},$$

$$W_{2,\mathsf{a},\mathsf{b}} = \frac{u_o^2 \sin{(k_p(\mathsf{a}-\mathsf{b}))}}{k_p(u_o^2 - v_o^2)} - \frac{v_o^2 \sin{(k_h(\mathsf{a}-\mathsf{b}))}}{k_h(u_o^2 - v_o^2)},$$

$$W_{3,\mathsf{a},\mathsf{b}} = \frac{u_o v_o \cos{(k_h(\mathsf{a}-\mathsf{b}))}}{(u_o^2 - v_o^2)} - \frac{u_o v_o \cos{(k_p(\mathsf{a}-\mathsf{b}))}}{(u_o^2 - v_o^2)},$$

$$W_{4,\mathsf{a},\mathsf{b}} = \frac{u_o v_o \sin{(k_h(\mathsf{a}-\mathsf{b}))}}{k_h(u_o^2 - v_o^2)} - \frac{u_o v_o \sin{(k_p(\mathsf{a}-\mathsf{b}))}}{k_p(u_o^2 - v_o^2)},$$

$$X_{1,\mathsf{a},\mathsf{b}} = \frac{k_h v_o^2 \sin{(k_h(\mathsf{a}-\mathsf{b}))}}{(u_o^2 - v_o^2)} - \frac{k_p u_o^2 \sin{(k_p(\mathsf{a}-\mathsf{b}))}}{(u_o^2 - v_o^2)},$$

$$X_{2,\mathsf{a},\mathsf{b}} = \frac{u_o^2 \cos{(k_p(\mathsf{a}-\mathsf{b}))}}{(u_o^2 - v_o^4)} - \frac{v_o^2 \cos{(k_h(\mathsf{a}-\mathsf{b}))}}{(u_o^2 - v_o^2)},$$

$$X_{3,\mathsf{a},\mathsf{b}} = \frac{k_p u_o v_o \sin{(k_p(\mathsf{a}-\mathsf{b}))}}{(u_o^2 - v_o^2)} - \frac{k_h u_o v_o \sin{(k_h(\mathsf{a}-\mathsf{b}))}}{(u_o^2 - v_o^2)},$$

$$X_{4,\mathsf{a},\mathsf{b}} = \frac{u_o v_o \cos{(k_h(\mathsf{a}-\mathsf{b}))}}{(u_o^2 - v_o^2)} - \frac{u_o v_o \cos{(k_p(\mathsf{a}-\mathsf{b}))}}{(u_o^2 - v_o^2)},$$

$$Y_{1,\mathsf{a},\mathsf{b}} = \frac{u_o v_o \cos{(k_p(\mathsf{a}-\mathsf{b}))}}{(u_o^2 - v_o^2)} - \frac{u_o v_o \cos{(k_h(\mathsf{a}-\mathsf{b}))}}{(u_o^2 - v_o^2)},$$

$$Y_{2,\mathsf{a},\mathsf{b}} = \frac{u_o v_o \sin{(k_p(\mathsf{a}-\mathsf{b}))}}{k_p(u_o^2 - v_o^2)} - \frac{u_o v_o \sin{(k_h(\mathsf{a}-\mathsf{b}))}}{k_h(u_o^2 - v_o^2)},$$

$$Y_{3,\mathsf{a},\mathsf{b}} = \frac{u_o^2 \cos{(k_h(\mathsf{a}-\mathsf{b}))}}{(u_o^2 - v_o^2)} - \frac{v_o^2 \cos{(k_p(\mathsf{a}-\mathsf{b}))}}{(u_o^2 - v_o^2)},$$

$$Y_{4,\mathsf{a},\mathsf{b}} = \frac{u_o^2 \sin{(k_h(\mathsf{a}-\mathsf{b}))}}{k_h(u_o^2 - v_o^2)} - \frac{v_o^2 \sin{(k_p(\mathsf{a}-\mathsf{b}))}}{k_p(u_o^2 - v_o^2)},$$

$$Z_{1,\mathsf{a},\mathsf{b}} = \frac{k_h u_o v_o \sin{(k_h(\mathsf{a}-\mathsf{b}))}}{(u_o^2 - v_o^2)} - \frac{k_p u_o v_o \sin{(k_p(\mathsf{a}-\mathsf{b}))}}{(u_o^2 - v_o^2)},$$

$$Z_{2,\mathsf{a},\mathsf{b}} = \frac{u_o v_o \cos{(k_p(\mathsf{a}-\mathsf{b}))}}{(u_o^2 - v_o^2)} - \frac{u_o v_o \cos{(k_h(\mathsf{a}-\mathsf{b}))}}{(u_o^2 - v_o^2)},$$

$$Z_{3,\mathsf{a},\mathsf{b}} = \frac{k_p v_o^2 \sin{(k_p(\mathsf{a}-\mathsf{b}))}}{(u_o^2 - v_o^2)} - \frac{k_h u_o^2 \sin{(k_h(\mathsf{a}-\mathsf{b}))}}{(u_o^2 - v_o^2)},$$

$$Z_{4,\mathsf{a},\mathsf{b}} = \frac{u_o^2 \cos{(k_h(\mathsf{a}-\mathsf{b}))}}{(u_o^2 - v_o^2)} - \frac{v_o^2 \cos{(k_p(\mathsf{a}-\mathsf{b}))}}{(u_o^2 - v_o^2)}.$$

APPENDIX C: SHOT-NOISE FORMULAS

The total shot noise was derived in Ref. [22] and can be written

$$\mathrm{S}_{\mathrm{tot}}^{LR} = \mathrm{S}_{pp}^{LR} + \mathrm{S}_{hh}^{LR} + \mathrm{S}_{ph}^{LR}, \tag{C1}$$

where

$$\mathrm{S}_{pp}^{LR} = \frac{m_L m_R}{\pi^2 \hbar^4} \int de \, dS_{pp}^{LR}(e), \quad \mathrm{S}_{hh}^{LR} = \frac{m_L m_R}{\pi^2 \hbar^4} \int de \, dS_{hh}^{LR}(e),$$

$$\mathrm{S}_{ph}^{LR} = \frac{m_L m_R}{\pi^2 \hbar^4} \int de \, dS_{ph}^{LR}(e) \tag{C2}$$

are the contributions to the shot noise due to particle-particle, hole-hole, and particle-hole correlations, respectively. The contributions to the differential shot noise, $dS_{pp}^{LR}(e)$, $dS_{hh}^{LR}(e)$, and $dS_{ph}^{LR}(e)$, are given below:

$$dS_{pp}^{LR}(e) = F_p^L N_p^L \big(\big(-\big|r_{hp}^{LL}\big|^2 + \big|r_{pp}^{LL}\big|^2 - 1 \big) \big(-\big|t_{hp}^{RL}\big|^2 + \big|t_{pp}^{RL}\big|^2 \big) \big) + F_p^R N_p^R \big(\big(-\big|r_{hp}^{RR}\big|^2 + \big|r_{pp}^{RR}\big|^2 - 1 \big) \big(-\big|t_{hp}^{LR}\big|^2 + \big|t_{pp}^{LR}\big|^2 \big) \big)$$

$$+ \big(F_p^L N_p^R + F_p^R N_p^L \big) \big(\mathrm{Re}\big[r_{hp}^{LL} r_{hp}^{RR} t_{hp}^{LR*} t_{hp}^{RL*}\big] - \mathrm{Re}\big[r_{hp}^{LL*} r_{pp}^{RR*} t_{pp}^{RL} t_{hp}^{LR}\big] + \mathrm{Re}\big[r_{pp}^{LL} r_{pp}^{RR} t_{pp}^{LR*} t_{pp}^{RL*}\big] - \mathrm{Re}\big[r_{pp}^{LL*} r_{hp}^{RR*} t_{hp}^{RL} t_{pp}^{LR}\big] \big), \tag{C3}$$

where $F_{p(h)}^{L(R)} = \big(1 - N_{p(h)}^{L(R)} \big)$,

$$dS_{hh}^{LR}(e) = F_h^L N_h^L \big(\big(\big|r_{hh}^{LL}\big|^2 - \big|r_{ph}^{LL}\big|^2 - 1 \big) \big(\big|t_{hh}^{RL}\big|^2 - \big|t_{ph}^{RL}\big|^2 \big) \big) + F_h^R N_h^R \big(\big(\big|r_{hh}^{RR}\big|^2 - \big|r_{ph}^{RR}\big|^2 - 1 \big) \big(\big|t_{hh}^{LR}\big|^2 - \big|t_{ph}^{LR}\big|^2 \big) \big)$$

$$+ \big(F_h^L N_h^R + F_h^R N_h^L \big) \big(\mathrm{Re}\big[r_{hh}^{LL} r_{hh}^{RR} t_{hh}^{LR*} t_{hh}^{RL*}\big] - \mathrm{Re}\big[r_{hh}^{LL*} r_{ph}^{RR*} t_{ph}^{RL} t_{hh}^{LR}\big] + \mathrm{Re}\big[r_{ph}^{LL} r_{ph}^{RR} t_{ph}^{LR*} t_{ph}^{RL*}\big] - \mathrm{Re}\big[r_{ph}^{LL*} r_{hh}^{RR*} t_{hh}^{RL} t_{ph}^{LR}\big] \big), \tag{C4}$$

and

$$
\begin{aligned}
dS_{ph}^{LR}(e) = & \left(F_h^L N_p^L + F_p^L N_h^L\right)\left(\mathrm{Re}\!\left[r_{hh}^{LL} r_{hp}^{LL*} t_{hp}^{RL} t_{hh}^{RL*}\right] - \mathrm{Re}\!\left[r_{hh}^{LL} r_{hp}^{LL*} t_{ph}^{RL*} t_{hp}^{RL}\right] - \mathrm{Re}\!\left[r_{ph}^{LL} r_{pp}^{LL*} t_{hh}^{RL*} t_{hp}^{RL}\right] + \mathrm{Re}\!\left[r_{ph}^{LL} r_{pp}^{LL*} t_{pp}^{RL} t_{ph}^{RL*}\right]\right) \\
& + \left(F_h^R N_p^R + F_p^R N_h^R\right)\left(\mathrm{Re}\!\left[r_{hh}^{RR} r_{hp}^{RR*} t_{hp}^{LR} t_{hh}^{LR*}\right] - \mathrm{Re}\!\left[r_{hh}^{RR} r_{hp}^{RR*} t_{ph}^{LR*} t_{pp}^{LR}\right] - \mathrm{Re}\!\left[r_{ph}^{RR} r_{pp}^{RR*} t_{hh}^{LR*} t_{hp}^{LR}\right] + \mathrm{Re}\!\left[r_{ph}^{RR} r_{pp}^{RR*} t_{pp}^{LR} t_{ph}^{LR*}\right]\right) \\
& + \left(F_h^L N_p^R + F_p^R N_h^L\right)\left(\mathrm{Re}\!\left[r_{hh}^{LL} r_{hp}^{RR} t_{hp}^{LR*} t_{hh}^{RL*}\right] - \mathrm{Re}\!\left[r_{hh}^{LL*} r_{pp}^{RR} t_{ph}^{RL} t_{hp}^{LR}\right] + \mathrm{Re}\!\left[r_{ph}^{LL} r_{pp}^{RR} t_{pp}^{LR*} t_{ph}^{RL*}\right] - \mathrm{Re}\!\left[r_{ph}^{LL*} r_{hp}^{RR} t_{hh}^{RL} t_{pp}^{LR}\right]\right) \\
& + \left(F_p^L N_h^R + F_h^R N_p^L\right)\left(\mathrm{Re}\!\left[r_{hp}^{LL} r_{hh}^{RR} t_{hh}^{LR*} t_{hp}^{RL*}\right] - \mathrm{Re}\!\left[r_{hp}^{LL*} r_{ph}^{RR*} t_{pp}^{RL} t_{hh}^{LR}\right] + \mathrm{Re}\!\left[r_{pp}^{LL} r_{ph}^{RR} t_{ph}^{LR*} t_{pp}^{RL*}\right] - \mathrm{Re}\!\left[r_{pp}^{LL*} r_{hh}^{RR*} t_{hp}^{RL} t_{ph}^{LR}\right]\right).
\end{aligned}
$$

$$\text{(C5)}$$

[1] M. Srednicki, Phys. Rev. E **50**, 888 (1994).

[2] J. M. Deutsch, Rep. Prog. Phys. **81**, 082001 (2018).

[3] L. E. Reichl, *The Transition to Chaos*, 3rd ed. (Springer Nature, Cham, Switzerland, 2021).

[4] J. Eisert, M. Friesdorf, and C. Gogolin, Nat. Phys. **11**, 124 (2015).

[5] A. M. Kaufman, M. E. Tai, A. Lukin, M. Rispoli, R. Schittko, P. M. Preiss, and M. Greiner, Science **353**, 794 (2016).

[6] M. Buttiker, P. Samuelsson, and E. V. Sukhorukov, Proc. of SPIE **5843**, 66 (2005).

[7] N. M. Chtchelkatchev, G. Blatter, G. B. Lesovik, and T. Martin, Phys. Rev. B **66**, 161320(R) (2002).

[8] P. Samuelsson, E. V. Sukhorukov, and M. Buttiker, Phys. Rev. Lett. **91**, 157002 (2003).

[9] A. Das, Y. Ronen, M. Heiblum, D. Mahalu, A. V. Kretinin, and H. Shtrikman, Nat. Commun. **3**, 1165 (2012).

[10] D. S. Golubev and A. D. Zaikin, Phys. Rev. B **82**, 134508 (2010)

[11] D. S. Golubev and A. D. Zaikin, Phys. Rev. B **99**, 144504 (2019).

[12] C. Ostrove and L. E. Reichl, Phys. B: Condens. Matter **561**, 79 (2019).

[13] L. E. Reichl, Phys. B: Condens. Matter **586**, 412114 (2020).

[14] M. Flöser, D. Feinberg, and R. Mélin, Phys. Rev. B **88**, 094517 (2013).

[15] R. Melin, F. S. Bergeret, and A. Levy Yeyati, Phys. Rev. B **79**, 104518 (2009).

[16] S. Duhot and R. Melin, Phys. Rev. B **77**, 014525 (2008).

[17] Z-Y. Zeng, L. Zhou, J. Hong, and B. Li, Phys. Rev. B **74**, 085312 (2006).

[18] M. P. Anantram and S. Datta, Phys. Rev. B **53**, 16390 (1996).

[19] G. Bignon, M. Houzet, F. Pistolesi, and F. W. J. Hekking, Europhys. Lett. **67**, 110 (2004).

[20] A. Freyn, M. Floser, and R. Melin, Phys. Rev. B **82**, 014510 (2010).

[21] A. Levy Yeyati, F. S. Bergeret, A. Martin-Rodero, and T. M. Klapwijk, Nat. Phys. **3**, 455 (2007).

[22] C. Ostrove and L. E. Reichl, Phys. Rev. B **103**, 224518 (2021).

[23] L. E. Reichl, Phys. B: Condens. Matter **628**, 413598 (2022).

[24] R. Ionicioiu, G. Amaratunga, and F. Udrea, Int. J. Mod. Phys. **15**, 125 (2001).

[25] S. Gazibegovic, D. Car, H. Zhang, S. C. Balk, J. A. Logan, M. W. A. deMoor, M. C. Cassidy, R. Schmits, D. Xu, G. Wang, P. Krogstrup, R. L. M. Op het Veld, K. Zuo, Y. Vos, J. Shen, D. Bouman, B. Shojaer, D. Pennachio, J. S. Lee, P. J. van Veldhoven, S. Koelling, M. A. Verheijen *et al.* Nature (London) **548**, 434 (2017).

[26] A. E. Hansen, A. Kristensen, S. Pedersen, C. B. Sorensen, and P. E. Lindelof, Phys. Rev. B **64**, 045327 (2001).

[27] V. Spicka, J. Masek, and B. Velicky, J. Phys.: Condens. Matter **2**, 1569 (1990).

[28] M. Cyrot and D. Pavuna, *Introduction to Superconductivity and High-T_c Materials* (World Scientific, Singapore, 1995).

[29] P. G. deGennes, *Superconductivity of Metals and Alloys* (CRC Press, Bocza Raton, 2018).

[30] A. F. Andreev, Sov. Phys. JETP **19**, 1228 (1962).

[31] L. E. Reichl, *A Modern Course in Statistical Physics*, 4th ed. (Wiley-VCH, Weinheim, 2016).

[32] E. Wigner, *Conference on neutron physics by time of flight, Gatlinburg, Tennessee, November 1956*, Oak Ridge Natl. Lab. Report No. ORNL-2309, p. 67. Reprinted in Ref. [33], p. 188.

[33] C. E. Porter, *Statistical Theories of Spectra: Fluctuations* (Academic Press, Cambridge, MA, 1965).

[34] F. J. Dyson, J. Math. Phys. **3**, 140 (1962); **3**, 166 (1962); **3**, 1191 (1962).

[35] C. H. Lewenkopf and H. A. Weidenmuller, Ann. Phys. **212**, 53 (1991).

[36] P. A. Mello, P. Pereyra, and T. H. Seligman, Ann. Phys. **161**, 254 (1985).

[37] P. W. Brouwer, Phys. Rev. B **51**, 16878 (1995).

[38] Ya. M. Blanter and M. Buttiker, Phys. Rep. **336**, 1 (2000).

[39] C. Beenakker and C. Schonenberger, Phys. Today **56**(5), 37 (2003).

[40] J. Torres and T. Martin, Eur. Phys. J. B **12**, 319 (1999).

[41] S. A. Hill and W. K. Wootters, Phys. Rev. Lett. **78**, 5022 (1997).

[42] W. K. Wootters, Phys. Rev. Lett. **80**, 2245 (1998).

[43] P. Rungta, V. Buzek, C. M. Caves, M. Hillery, and G. J. Milburn, Phys. Rev. A **64**, 042315 (2001).